THE JOURNAL OF PHYSICAL CHEMISTRY C

Article

Cite This: J. Phys. Chem. C 2019, 123, 19748−19758

pubs.acs.org/JPCC

Design, Synthesis, and Characterization of Metal−Organic Frameworks for Enhanced Sorption of Chemical Warfare Agent Simulants

Jonathan P. Ruffley,[†,∥] Isabella Goodenough,[§,∥] Tian-Yi Luo,[‡,∥] Melissandre Richard,[§,⊥] Eric Borguet,[*,§] Nathaniel L. Rosi,[*,†,‡] and J. Karl Johnson[*,†]

[†]Department of Chemical and Petroleum Engineering and [‡]Department of Chemistry, University of Pittsburgh, Pittsburgh, Pennsylvania 15261, United States

[§]Department of Chemistry, Temple University, Philadelphia, Pennsylvania 19122, United States

Supporting Information

ABSTRACT: Metal−organic frameworks (MOFs) and specifically the UiO family of MOFs have been extensively studied for the adsorption and degradation of chemical warfare agents (CWAs) and their simulants. We present a combined experimental and computational study of the adsorption of dimethyl methylphosphonate (DMMP), a CWA adsorption simulant, in functionalized UiO-67. We have used density functional theory (DFT) to design functionalized MOFs having a range of binding energies for DMMP. We have selected three different functionalized MOFs for experimental synthesis and characterization from a total of eight studied with DFT. These three MOFs were identified as having the weakest, intermediate, and strongest binding energies for DMMP of the set, as predicted by our DFT calculations. We find that the order of predicted binding energies agrees with data from temperature-programmed desorption experiments. Moreover, the values of the binding energies are also in good agreement. This serves as a proof of concept that ab initio calculations can guide experiments in designing MOFs that exhibit a higher affinity for CWAs and their simulants. One surprising outcome of this work is that reactions between DMMP and the three functionalized UiO-67 MOFs were not observed under ultrahigh-vacuum conditions for the exposure of DMMP of up to 9000 L. This lack of reactivity is attributed to the low levels of defects in the materials used.

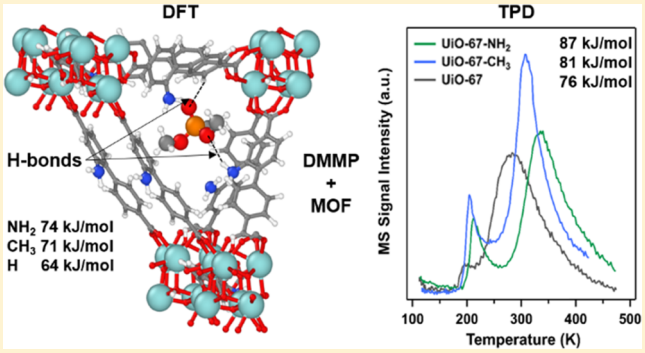

INTRODUCTION

Chemical warfare agents (CWAs) are a persistent and evolving threat. Therefore, the continued development of mitigation and defense technologies is necessary. Currently, a combination of high-efficiency particulate air filtration media and activated carbon impregnated with materials capable of reacting with volatile species is used in respirators to protect against exposure to CWAs.[1−3] While highly effective in capturing a variety of deadly species, microporous carbon-based materials suffer from limited selectivity to CWAs due to their ill-defined pore sizes, shapes, and pore chemistry.[4] In addition, the lack of catalytic activity in purely carbonaceous sorbents (e.g., activated carbon) results in the potential re-emission of CWAs.[5,6]

Key features of an ideally reactive sorbent material for CWA removal include high capacity and selectivity toward CWAs, the ability to convert CWAs into benign products, stability under a variety of conditions for a long period of time, and the ability to regenerate the sorbent and catalyst. To this end, metal−organic frameworks (MOFs) have many advantages. Compared to porous carbons, many MOFs have not only larger surface areas for high adsorption capacity but also well-defined pores required for high selectivity.[7,8] Further, MOF pore dimensions and chemistry can be systematically modified by adjusting the size and functional groups of organic linkers, which can significantly affect MOF−adsorbate interactions and potentially lead to enhanced selectivity for specific adsorbates.[9,10]

A variety of MOFs have been examined for CWA simulant adsorption and destruction.[11−16] Computational and experimental methods demonstrate that MOFs degrade CWAs and less hazardous CWA simulant molecules in acidic/basic/neutral solutions,[11,12,17−20] under ambient conditions,[21,22] catalytically,[11,12,17−20,22−24] noncatalytically,[21] when impregnated into other materials such as textiles,[20,24,25] and when doped or impregnated with other materials, such as Lewis bases.[19,23]

Received: June 11, 2019
Revised: July 19, 2019
Published: July 22, 2019

DOI: 10.1021/acs.jpcc.9b05574
J. Phys. Chem. C 2019, 123, 19748−19758

Chart 1. Ligands Computationally Screened To Create a UiO-67 MOF Family[a]

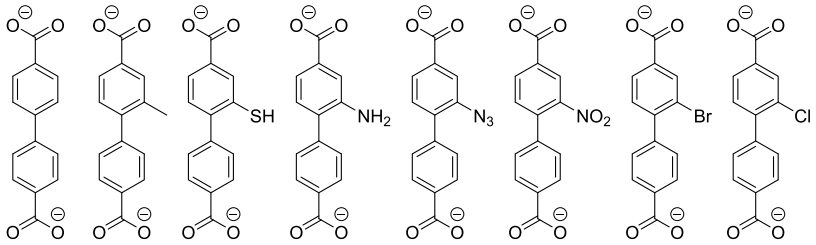

[a]From left to right: BPDC, CH_3-BPDC, SH-BPDC, NH_2-BPDC, N_3-BPDC, NO_2-BPDC, Br-BPDC, Cl-BPDC.

In this work, we focus on the UiO family of MOFs.[26] These MOFs consist of $Zr_6O_4(OH)_4(COO)_{12}$ secondary building units (SBUs) interconnected by linear dicarboxylate ligands and are known for their exceptional thermal, mechanical, and chemical stabilities.[26−28] By introducing functional groups to the ligands presynthesis, numerous variations of these MOFs have been synthesized while maintaining excellent stability properties.[29−32]

Recently, Wang et al. reported that dimethyl methylphosphonate (DMMP), an adsorption simulant for sarin, can be adsorbed by nonfunctionalized Zr-based MOFs via both reversible physisorption and irreversible chemisorption.[21] However, there have been relatively few studies of the interactions of CWAs or CWA simulants with functionalized MOFs.[33] Our hypothesis is that different functional groups incorporated into MOF linkers can be used to tune the adsorption strength of CWAs. At the outset, it is not obvious that CWA or simulant adsorption strengths can be controlled through modifying the linker with different functional groups because these molecules typically interact strongly with the SBU rather than the linker.[21,34] However, the strong guest−SBU interactions are typically due to the presence of defects, such as missing linkers;[21,34,35] we assume that in relatively defect-free MOFs the sorbent−sorbate interactions can be tuned by introducing functional groups on the linker.

This work examines the adsorption of DMMP in functionalized UiO-67 with the goal of identifying functional groups that impart enhanced MOF−DMMP binding. We use a variety of experimental and computational methods to probe three functionalized UiO-67 MOFs, determining the nature of their interactions with DMMP. The studies and conclusions presented herein will inform our design of stratified MOFs[36] containing specific domains that selectively concentrate CWAs and others that reject undesired background molecules and/or enhance the removal of CWA degradation products.

EXPERIMENTAL AND THEORETICAL METHODOLOGY

Functional Group Identification. We selected UiO-67 as the platform MOF for our studies because its pore windows are sufficiently large to permit the facile diffusion of CWAs and their simulants.[21] We note, however, that the stability of the UiO MOFs generally decreases with increasing ligand size;[27,37] UiO-67 is an appropriate selection to balance stability and pore size concerns. It has been shown that UiO-67 is not stable in the presence of water vapor;[38] however, the synthesis procedure used[39] is different from that used here, and reactivity with water may depend on the synthesis used, assuming that the reactivity is defect-driven.

We confined our search for functional groups to a subset of those that have already been incorporated within UiO-6x MOFs.[29,40−42] Specifically, we considered the ligands shown in Chart 1, derivatized from 1,1′-biphenyl-4,4′-dicarboxylate (BPDC) with different substituents at the 2-position, including −H, $-CH_3$, −SH, $-NH_2$, $-N_3$, $-NO_2$, −Br, and −Cl. We denote the corresponding UiO-67 analogue MOFs as UiO-67-X, where X represents the functional moiety.

As an initial screening of the binding of DMMP with the functionalized MOFs, benzene was used to represent the BPDC linker. Binding energies of DMMP with functionalized benzene were considered as a surrogate for the binding energies of DMMP in the UiO-67-X MOFs. The ABCluster[43,44] program was used to generate 20 random configurations of DMMP around the functionalized benzene rings to identify the ground-state binding configurations. These configurations were then optimized using density functional theory (DFT), as implemented in Orca.[45] Convergence criteria are reported in Table S1 of the Supporting Information. The Perdew−Burke−Ernzerhof functional[46] was used with the Def2-TZVP basis set[47,48] and the D3BJ dispersion correction.[49,50] The resulting energies were checked for basis set superposition error via the Boys−Bernardi counterpoise correction,[51] as implemented in Gaussian 09,[52] shown in Table S2. The level of theory was verified to give appropriate results for the systems of interest by comparing the DFT results with the delocalized pair natural orbital-coupled cluster single double perturbational triple (DLPNO-CCSD(T))[53] calculations, shown in Figure S1. A single DMMP molecule, as well as each of the functionalized benzene molecules, was relaxed following this same procedure. The resulting energies were then used to calculate binding energies via eq 1

$$\Delta E_{\text{bind}} = E_{\text{AB}} - E_{\text{A}} - E_{\text{B}} \quad (1)$$

Note that ΔE_{bind} is negative if the binding is favorable. The functionalized linkers were incorporated into perfect UiO-67 primitive cells. The atom positions (included in the SI), using lattice parameters of relaxed UiO-67 ($a = b = c = 19.1$ Å, $\alpha = \beta = \gamma = 60°$), were then relaxed using DFT as implemented in CP2K.[54−56] The lattice parameters of each MOF were not relaxed because it has been shown that there is minimal difference between the parameters of MOFs with different functional groups.[57] The Goedecker−Teter−Hutter pseudopotentials[58] were used with the DZVP-MOLOPT-SR basis set,[59] and Grimme's D3 dispersion correction[49] was applied. The cutoff and relative cutoff were 400 and 50 Ry, respectively. Convergence information is included in Figures S2 and S3 of the Supporting Information. The DIIS orbital transformation minimizer[56] and LBFGS optimizer[60] were used. These settings were used for all other CP2K calculations in this work. A single

DOI: 10.1021/acs.jpcc.9b05574
J. Phys. Chem. C 2019, 123, 19748−19758

gas-phase DMMP molecule was also relaxed using this procedure to compute binding energies.

The ground state of a single DMMP molecule in the various UiO-67-X MOFs was estimated using the following procedure: a single DMMP molecule was randomly placed into the octahedral pore of each primitive cell. Ab initio molecular dynamics (AIMD) simulations in the canonical ensemble were carried out on the periodic system at a temperature of 1000 K using the GLE thermostat.[61,62] The AIMD simulations were run for 7.5 ps, using a time step of 0.5 fs. The coordinates of the AIMD simulations were saved every 100 time steps, and the sampled geometries were relaxed in CP2K to their local minima. The lowest-energy structure identified was used in eq 1 to compute the binding energy for each functionalized MOF. Strongest binding energy structures for each MOF were then retested by substituting functional groups for all other MOFs into these structures as additional configurations.

MOF Synthesis and Characterization. Based on the DFT calculations, amino- and methyl-functionalized linkers were chosen to give strong and intermediate binding energies with DMMP, respectively, while the unfunctionalized biphenyl linker was chosen to give weak binding. Monocrystalline samples of UiO-67-NH_2, UiO-67-CH_3, and UiO-67 containing discrete crystallites were synthesized by reacting 2-amino-1,1′-biphenyl-4,4′-dicarboxylic acid, 2-methyl-1,1′-biphenyl-4,4′-dicarboxylic acid, and 1,1′-biphenyl-4,4′-dicarboxylic acid with zirconium precursors under solvothermal conditions, respectively. All purchased chemicals were used without further purification except where otherwise noted. Detailed procedures for ligand and MOF syntheses can be found in the Supporting Information.

Powder X-ray diffraction (PXRD) patterns were collected using a Bruker AXS D8 discover powder diffractometer at 40 kV, 40 mA for Cu Kα (λ = 1.5406 Å) with a scan speed of 0.10 s/step from 3 to 45° at a step size of 0.02°. The data were analyzed using the EVA program from the Bruker powder analysis software package. The simulated powder patterns were calculated using Mercury 3.8, based on the crystal structure of UiO-67.

N_2 gas adsorption experiments were performed using a Quantachrome Autosorb-1 instrument. MOF samples suspended in dimethyl formamide (DMF) were centrifuged at 5000 rpm for 3 min. After the removal of the supernatant, the precipitate was evacuated on a Schlenk line for 20 min. The powdery sample was then activated by heating under vacuum at an outgassing station on a Quantachrome Autosorb-1 instrument in three sequential stages: 50 °C for 1 h, 90 °C for 2 h, and 100 °C for 15 h. N_2 adsorption isotherms at 77 K were then collected.

Elemental microanalyses were performed by the University of Illinois, Department of Chemistry Microanalytical Laboratory, using a PerkinElmer 240 elemental analyzer and an Exeter analytical CE440. Prior to the analysis, MOF samples were activated under vacuum on an Autosorb AS-1 (vide supra) and shipped to the microanalytical laboratory.

Thermogravimetric analyses (TGA) were performed using a TGA Q500 thermal analysis system under a nitrogen atmosphere from room temperature to 650 °C at a ramping rate of 5 °C/min.

Transmission electron microscopy (TEM) imaging was conducted on an FEI Morgagni 268 operated at 80 kV and equipped with an AMT side mount CCD camera system. TEM samples were prepared by drop-casting 3 μL of ethanol suspension of a MOF sample onto a 3 mm diameter copper grid with carbon/formvar coating. The grid was then air-dried before TEM imaging.

Simulated surface areas were calculated for each MOF using a Lennard-Jones 12−6 argon model[63] following an accessible surface area procedure[64] and compared to Brunauer−Emmett−Teller (BET)[65] surface areas calculated from nitrogen isotherms at 77 K. These nitrogen isotherms were compared to isotherms simulated within the grand canonical Monte Carlo (GCMC) approach, as implemented in RASPA.[66] The potential used for nitrogen was taken from the literature.[67]

DMMP Force Field. Existing classical force fields for DMMP have been reported in the literature.[68,69] However, we chose to develop a fully flexible force field with intramolecular potential parameters for DMMP generated by the QuickFF formalism.[70] Our force field is based on model 2 from Vishnyakov and Neimark,[69] with corrected charges. Details of the procedure are given in the Supporting Information. We chose this approach to facilitate the rapid generation of force fields for other simulants and CWAs to be used in molecular dynamics simulations.

A Lennard-Jones and Coulomb model was used for nonbonded interactions. Electrostatic parameters were corrected to achieve charge neutrality while producing a physically reasonable dipole moment for DMMP.[71] Lennard-Jones parameters were adjusted to reproduce the liquid density of DMMP at 298 K and 1 atm. Ewald summation[72] was used to calculate electrostatic interactions. Lorentz−Berthelot combining rules were used for unlike interactions. Intramolecular interactions involving atoms separated by less than four bonds were excluded. Molecular dynamics simulations were performed using LAMMPS[73] in the isothermal−isobaric ensemble.[74] These results were compared to isothermal−isobaric Monte Carlo simulations performed in RASPA[66] to validate the potential. Initial configurations for LAMMPS simulations were created with Packmol.[75] Additional details of these simulations are reported in Tables S3 and S4 of the Supporting Information. DMMP force field parameters are given in Tables S5−S8 of the Supporting Information.

Simulated Isotherms. Excess adsorption isotherms of nitrogen at 77 K and absolute isotherms of DMMP at 298 K were simulated in the three UiO-67-X MOFs from GCMC simulations, using the RASPA[66] software package. Density-derived electrostatic and chemical (DDEC) charges for the atoms in each MOF were computed using the DDEC6[76−79] formalism. Ewald summation[72] was used to calculate all electrostatic interactions. The Lennard-Jones parameters for the MOF atoms were taken from DREIDING,[80] except zirconium, which was sourced from UFF,[81] as has been done previously.[82] The potential was truncated at a cutoff of 14.0 Å, and standard tail corrections were applied.[83] Lorentz−Berthelot combining rules were used for unlike interactions. Helium void fractions were calculated for each MOF (Table S9), and the ideal gas Rosenbluth weight of DMMP was calculated to be 0.00556.[66] A supercell containing eight primitive cells with fixed MOF atoms was used for all GCMC simulations. One cycle was defined as N steps, where N was the number of adsorbates in the system at the beginning of the cycle. Each state was run for 5×10^4 equilibration cycles and 2×10^5 production cycles.

Experimental DMMP Binding Energies. Temperature-programmed desorption-mass spectrometry (TPD-MS) and

DOI: 10.1021/acs.jpcc.9b05574
J. Phys. Chem. C 2019, 123, 19748−19758

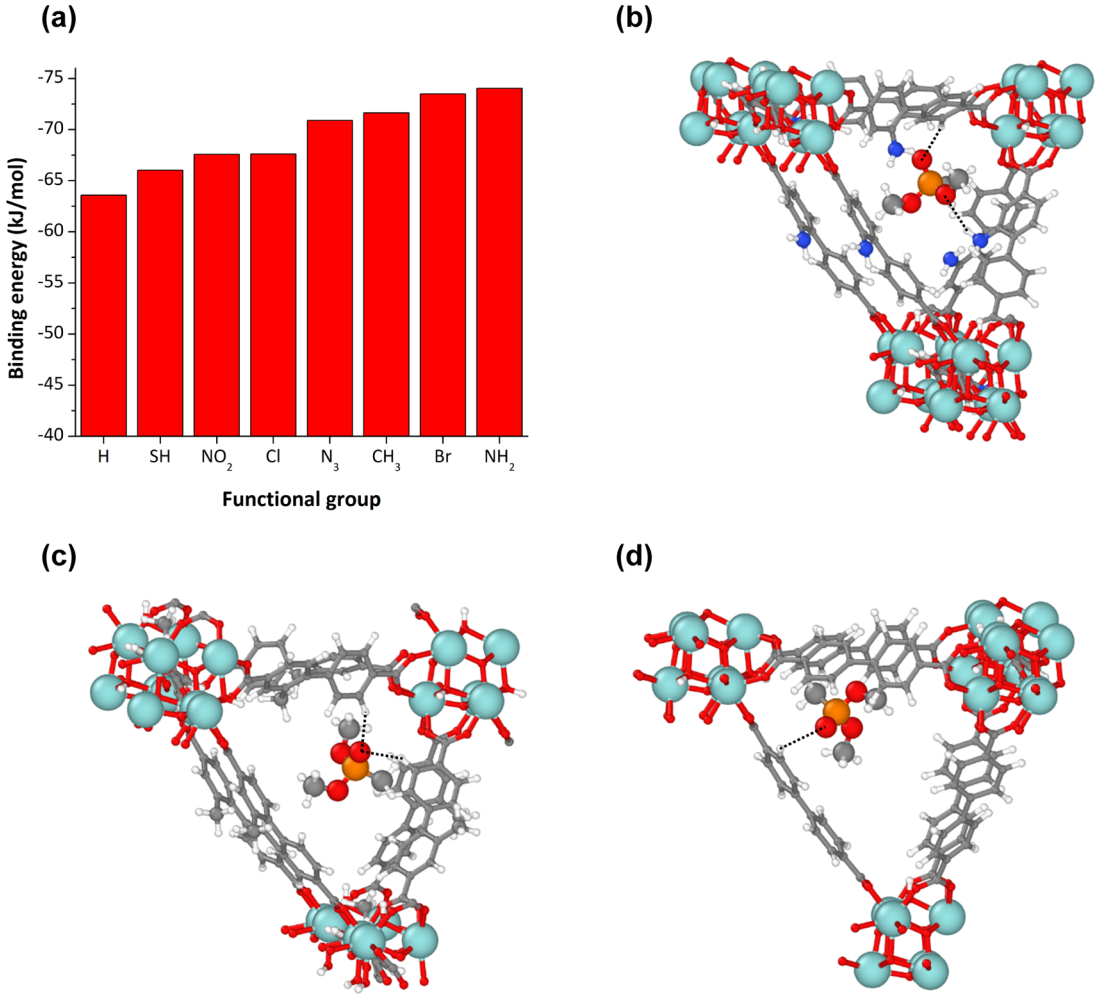

Figure 1. (a) Crystal binding energies computed from CP2K DFT calculations. (b) Optimal binding geometry of DMMP with UiO-67-NH_2. Dashed lines indicate hydrogen bonds of 2.34 Å (top) and 2.45 Å (bottom). (c) Optimal binding geometry of DMMP with UiO-67-CH_3. Dashed lines indicate hydrogen bonds of 2.28 Å (vertical) and 2.40 Å (horizontal). (d) Optimal binding geometry of DMMP with UiO-67. Dashed line indicates a hydrogen bond of 2.76 Å. For panels (b)−(d), Zr is shown in light blue, phosphorous shown in orange, oxygen shown in red, carbon shown in gray, nitrogen shown in blue, and hydrogen shown in white. Visualizations were created with OVITO.[85]

temperature-progammed infrared (TP-IR) experiments were performed in an ultrahigh-vacuum (UHV) instrument described previously.[84] Briefly, a stainless steel UHV chamber was evacuated using a turbomolecular pump backed by a mechanical pump providing a base pressure of less than 5×10^{-9} Torr after bakeout. MOF samples were deposited onto a clean 25 μm tungsten grid (AlfaAesar) braced to a copper sample manipulator. A fast-response K-type thermocouple (Omega) was spot-welded directly onto the tungsten (W) grid to monitor the sample temperature. This design allowed for rapid cooling of the sample to cryogenic temperatures of ∼100 K and resistive heating of up to 1400 K using direct current from a power supply (model # SCR 10-80, Electronic Measurements Inc.).

The MOF samples, dispersed in DMF, were first centrifuged at 14 000 rpm for 5 min, after which the supernatant solvent was removed. The wet MOF paste (∼2 mg) was placed onto the W grid using a spatula, and the paste adhered to the grid naturally as it dried. The sample was positioned in the center of the mesh as a disk of 6−8 mm diameter and a thickness of about 25−50 μm to provide uniform coverage with no apparent holes and introduced into the UHV chamber. The resulting optical density evaluated by Fourier transform infrared (FTIR) was on the order of 1. The chamber was baked out over a period of 18−24 h, during which the temperature of the sample and chamber reached a maximum of 373 K. Sample activation was achieved postbakeout by holding UiO-67 and UiO-67-NH_2 samples at 473 K for 1 h. UiO-67-CH_3 was held for 1 h at 473 K for IR experiments or 423 K for TPD experiments because the activation of UiO-67-CH_3 at 473 K resulted in reproducibility issues that were not seen for the other MOFs (Figure S4 in the Supporting Information).

DMMP (97% Sigma-Aldrich) vapor was dosed to the sample by backfilling the UHV chamber through a leak valve (Varian). The purity of DMMP was verified, after having undergone five freeze−pump−thaw cycles, using a shielded residual gas analyzer (RGA) (AccuQuad RGA 300, Stanford Research Systems) installed in the UHV chamber. Desired exposures of DMMP were achieved by dosing at a suitable constant pressure (typically 5×10^{-6} Torr), monitored with a nude ion gauge (Duniway iridium filament), for the time required to achieve the selected exposure, and measured in Langmuir, L, where 1 L = exposure of 10^{-6} Torr for 1 s. After DMMP adsorption at 100 K, the sample temperature was ramped at ∼2 K/s from 100 to 473 K (423 K for UiO-67-CH_3). The most abundant mass fragments of DMMP (m/z =

DOI: 10.1021/acs.jpcc.9b05574
J. Phys. Chem. C 2019, 123, 19748−19758

15, 79, 94, and 109) were monitored as a function of temperature during the TPD-MS experiment. A custom program written in LabVIEW, using drivers for commercial components, was used to control the heating process, monitor temperature and pressure, and track the evolution of selected mass fragments. To monitor DMMP integrity and purity, the mass spectra in the range of 1−130 amu were collected prior to experiments (Figure S5).

In situ IR was used to monitor changes in the MOF samples induced by DMMP by collecting spectra in real time using an FTIR spectrometer (Tensor 27, Bruker) via OPUS 7.5 software (Bruker). Spectra were recorded in transmission mode between 400 and 4000 cm^{-1} using a room-temperature DLaTGS detector with 4 cm^{-1} resolution and an average of 16 scans (6 mm aperture and 10 kHz scan velocity). Before each experiment, a 64-scan background spectrum was collected using the bare W mesh as the sample reference.

RESULTS AND DISCUSSION

Functional Group Selection. Binding energies for DMMP on periodic crystal models of UiO-67-X for X = H (unfunctionalized), CH_3, SH, NH_2, N_3, NO_2, Br, and Cl are shown in Figure 1a. The strongest binding energy for each pair is plotted. A parity plot of binding energies computed from crystal and cluster models is given in Figure S6 of the Supporting Information; trends in binding energies do not agree for the crystal and cluster calculations. The order from weakest to strongest binding for the crystal model is H < SH < Cl ∼ NO_2 < N_3 < CH_3 < Br < NH_2. The cluster binding energies are ordered from the weakest to strongest as H < Cl < Br < N_3 < CH_3 < NO_2 < SH < NH_2. Both models agree that H is the weakest, NH_2 is the strongest, and CH_3 is intermediate. We therefore chose these three materials for experimental study. UiO-67-CH_3 has not been previously reported in the literature, although UiO-66-CH_3 has been synthesized.[31] The geometries of the most favorable binding configurations for these three materials are also shown in Figure 1.

Examination of the local energy minima of DMMP and the crystal MOF model reveals that DMMP interacts with the confluence of linkers around the SBU of the MOF in each case (Figures 1 and S7−S14). This demonstrates that while functionalization of the ligand indeed appears to impact the binding energy of the MOF, the cluster model is not appropriate for making binding strength predictions; even if it produced substantially better agreement with the crystal model than that observed here, it is not an accurate physical representation of the interaction of interest, that of DMMP in an environment with several linkers. It is important to note that the DMMP does not interact directly with the SBU in the absence of missing linker defects, as can be seen from the closest pairwise interactions between DMMP and the framework coming from O atoms on DMMP interacting with H atoms on the linkers (Figure 1). It is also instructive to note that DMMP does not directly interact with the CH_3 functional group in UiO-67-CH_3, as can be seen from Figure 1c. We surmise that the CH_3 group provides steric and van der Waals interactions that increase the binding energy of DMMP relative to some other functional groups.

MOF Synthesis and Characterization. UiO-67-NH_2, UiO-67-CH_3, and UiO-67 were synthesized under solvothermal conditions as discrete crystallites (Figure S15). The phase purity of MOFs was verified by their powder X-ray diffraction (PXRD) patterns, which show good agreement with the PXRD pattern simulated from single-crystal diffraction data of UiO-67 (Figure S16). To determine the optimal sample activation conditions for TPD experiments, TGA was used to evaluate the thermal stability of three UiO-67 MOF analogues. TGA plots of all three as-synthesized samples (Figure S17) showed initial weight losses below 150 °C corresponding to the removal of solvent guests and negligible weight losses between 150 and 400 °C, indicating that all three samples may be thermally stable below 400 °C. Upon activation under vacuum at 100 °C, UiO-67-NH_2, UiO-67-CH_3, and UiO-67 samples exhibit type I nitrogen isotherms at 77 K (Figure S18), as expected for a microporous material.[86] Calculated helium void volumes followed the expected relative trend based on the functional group size (Table S9). The simulated isotherm is too attractive at moderate pressures but correctly captures the trends in adsorption as a function of pressure. It also accurately predicts loading at saturation. Further, there is no hysteresis in the experimental isotherms, as indicated by the coincidence of the adsorption and desorption branches. Experimental and simulated BET surface areas for these MOFs are in good agreement (Figure S19). This good agreement in surface areas indicates that the effects of missing linker defects present in the actual samples[35,42] are probably small. According to C, H, N microanalysis data of the MOF samples after solvent removal, UiO-67-NH_2, UiO-67-CH_3, and UiO-67 can be formulated as $Zr_6O_4(OH)_4(BPDC\text{-}NH_2)_{5.5}(OH)(H_2O)$, $Zr_6O_4(OH)_4(BPDC\text{-}CH_3)_{5.2}(OH)_{1.6}(H_2O)_{1.6}$, and $Zr_6O_4(OH)_4(BPDC)_{5.6}(OH)_{0.8}(H_2O)_{0.8}$, respectively. Compared to the formula of an ideal UiO-67 sample, which is $Zr_6O_4(OH)_4(BPDC\text{-}X)_6$, the synthesized MOF samples contain slightly fewer linkers. However, the microanalysis formulae indicate that the number of defects is similar in each sample. Therefore, the comparison of experimental results between samples should still reflect the effect of different functional groups.

Simulated DMMP Adsorption Isotherms. It is not possible to measure adsorption isotherms of DMMP with our adsorption instrument. We are, however, able to simulate adsorption isotherms of DMMP in the three MOFs at 298 K using the GCMC method. Our simulated isotherms are shown in Figure 2. At low pressures, the amount adsorbed follows the

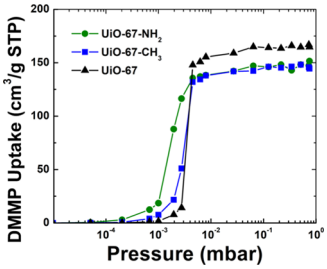

Figure 2. Absolute adsorption isotherms computed from GCMC simulations for DMMP at 298 K in UiO-67-NH_2, UiO-67-CH_3, and UiO-67.

binding energy trends predicted by DFT calculations. This is reasonable because the adsorbate−adsorbent interactions are expected to be dominated by the most attractive binding sites at low coverage. At higher loading, the surface area is the dominating factor in adsorption, following the trend predicted by the BET analysis and surface area calculations (Figure S19). A logistic 3P function was fit to each isotherm, and statistical

DOI: 10.1021/acs.jpcc.9b05574
J. Phys. Chem. C 2019, 123, 19748−19758

analysis was conducted. The results of this analysis, tabulated in Tables S10−S14, indicate that the differences in isotherms for the MOFs are statistically significant.

Experimental Binding of DMMP to the UiO-67-X Series MOFs. To investigate the strength and nature of adsorbate interactions with the UiO-67-X MOFs, TPD experiments were performed by monitoring the m/z = 15, 79, 94, and 109 DMMP molecular ion fragments as the MOF samples were heated under vacuum (from a base pressure <5 × 10^{-9} Torr) following analyte exposure. Similar temperature profiles shown in Figure S20 were obtained for all tracked masses for each exposure (1000−8000 L), providing evidence for the molecular desorption of DMMP from the different UiO-67-X MOFs investigated in this study. This result suggests that the association of DMMP with the MOF occurs primarily through physisorption. Previously, DMMP decomposition has been reported upon interaction with UiO-67 through hydrolysis of a single P−OCH_3 bond forming the chemisorbed Zr-bound product, methyl methylphosphonic acid, and methanol.[21] The lack of any significant evolution of methanol, as indicated by the molecular ion fragment (m/z = 32), from the full-mass spectrum (1−130 amu) shown in Figure S21, taken during heating after a 1000 L DMMP exposure provides further evidence of DMMP physisorption, rather than chemisorption.[87,88] This lack of chemisorption and reaction of DMMP is likely due to the low level of defects in our materials, combined with the absence of significant amounts of adsorbed water. The peak at m/z = 32 (Figure S21) is likely residual O_2, as this feature also appears in the pure DMMP spectrum prior to heating. This feature does not change significantly during heating, making it unlikely that the feature originates from evolving methanol caused by DMMP degradation.

The positions of each of the multiple peaks in the DMMP TPD spectra, shown in Figure 3, reflect the binding energy for the associated adsorption sites on the MOF. All spectra are shown for the m/z = 79 molecular ion, which is assigned to $PO_2CH_4^+$.[88,89] At the lowest DMMP exposure (1000 L), two desorption sites were observed for all UiO-67-X. The first site (M) (T < 230 K) evolved with a seemingly common leading edge and nonsymmetric peak shape with successive increases in exposure. This behavior typically reflects a process following zero-order kinetics, otherwise known as multilayer (M) desorption.[90,91] The second, higher-temperature site is more intense relative to the M-site and presents with a slightly nonsymmetrical peak shape. We assign this feature to strongly (S) physisorbed DMMP within the MOF. Increasing exposure beyond 2000 L leads to the appearance of a third, intermediate site, which we designate as weakly (W) physisorbed DMMP. For UiO-67-NH_2 and UiO-67, W- and S-physisorbed sites evolve as a single convoluted feature, whereas for UiO-67-CH_3, the W- and S-sites are distinct, well-resolved features in the TPD (Figure 3). We interpret S-site desorption to be DMMP-bound to the most easily accessible sites within the interior pore space. As exposure is increased, the saturation of higher-energy sites (S) allows for DMMP to populate lower-energy binding sites, giving rise to the W-site.

At the lowest DMMP exposure (1000 L), the W-site is not observed, as seen in Figure 4. The peak desorption temperature of the S-site of UiO-67-NH_2 (335 K) is greater than that of UiO-67-CH_3 (307 K) and UiO-67 (260 K), indicating that UiO-67-NH_2 has the strongest interaction with DMMP at low exposure. Unlike UiO-67-NH_2 or UiO-67, a

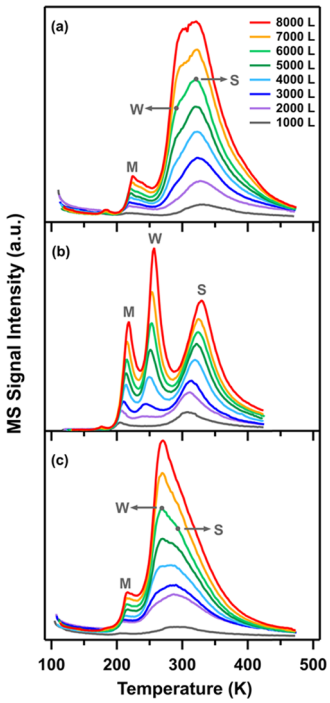

Figure 3. Thermal desorption profiles as a function of DMMP exposure for (a) UiO-67-NH_2, (b) UiO-67-CH_3, and (c) UiO-67. Spectra are shown for increasing exposure from 1000 L (gray) to 8000 L (red). Desorption sites are characterized by increasing temperature: (M) multilayer, (W) weakly physisorbed, and (S) strongly physisorbed.

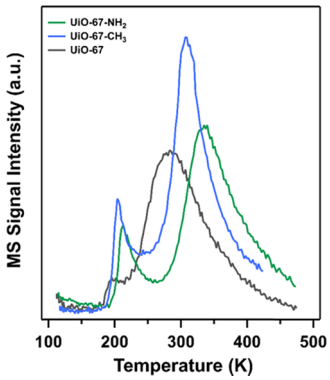

Figure 4. Thermal desorption profiles at a 1000 L DMMP exposure for UiO-67-NH_2 (green), UiO-67-CH_3 (blue), and UiO-67 (black).

significant coverage dependence is observed on the S-site of UiO-67-CH_3, where attractive interadsorbate interactions shift the peak toward a higher temperature with increased exposure. We have not been able to identify the origin of this shift.

The binding energies for the physisorbed DMMP species were calculated using the Redhead analysis method.[92] At low exposure (1000 L), the majority of DMMP is anticipated to initially adsorb to external surface sites and thus effects resulting from diffusion are neglected. Quantitative analysis was performed using the Polyani−Wigner eq 2,[93] where the desorption rate (r_{des}) is expressed by an nth order rate law

$$r_{des} = -\frac{d\theta}{dt} = \nu(\theta)\theta^n \exp\left[-\frac{E_{des}(\theta)}{RT_m}\right] \quad (2)$$

DOI: 10.1021/acs.jpcc.9b05574
J. Phys. Chem. C 2019, 123, 19748−19758

where θ is the coverage, $\nu(\theta)$ is the pre-exponential factor, n is the desorption order, $E_{des}(\theta)$ (kJ/mol) is the desorption energy, R is the ideal gas constant, and T_m (K) is the peak desorption temperature. Redhead derived a simple relationship between the desorption energy (E_{des}) and the peak desorption temperature (T_m) for the case where desorption follows first-order kinetics ($n = 1$) by assuming that the kinetic parameters are independent of surface coverage. The assumption of first-order kinetics for our TPD spectra is based on the asymmetric peak shapes with common leading edges seen in Figure 3. We also note that T_m is essentially independent of temperature for UiO-67-NH_2 and UiO-67 (Figure 3a,c, respectively). However, the strongly physisorbed peak of UiO-67-CH_3 varies slightly with the temperature at higher coverages but is independent of temperature for coverages from 1000 to 3000 L. Substituting $\frac{d\theta}{dt}\frac{dt}{dT}$ for $\frac{d\theta}{dT}$ and assuming that spectra were collected at a constant heating rate $\left(\beta = \frac{dT}{dt}\right)$ yield eq 3

$$\Delta E_{des} = RT_m\left[\ln\left(\frac{\nu \cdot T_m}{\beta}\right) - 3.46\right] \quad (3)$$

from which the energy of desorption can readily be extracted. In this work, the pre-exponential factor is assumed to be on the order of 10^{13} s^{-1}, a value typical for a process following first-order kinetics.[94]

The desorption profiles for a 1000 L DMMP exposure suggest the relative binding strength for the S-site as UiO-67-NH_2 > UiO-67-CH_3 > UiO-67 (Figure 4). Extracted energies from the S-site yield values of 87, 81, and 76 kJ/mol, respectively (Table 1). The energy trend compares quite favorably with the binding energies calculated from DFT on the periodic crystal, with the DFT giving weaker binding than the experiments by around 10 kJ/mol.

Table 1. Kinetic Parameters Extracted from Desorption Profiles Following 1000 L DMMP on UiO-67-X, Along with DFT Predictions of the Negative of the Binding Energies

MOF	T_{des}[a] (K)	E_{des} (kJ/mol)	E_{DFT} (kJ/mol)
UiO-67-NH_2	334	87 ± 2.0	74
UiO-67-CH_3	307	81 ± 0.5	71
UiO-67	260	76 ± 2.0	64

[a] T_{des} shown for single TPD spectra at a 1000 L DMMP exposure with a heating rate of 2.2 K/s.

Infrared spectroscopy as a function of exposure provides additional information on the uptake of DMMP by the MOF, the interadsorbate, and/or adsorbate−MOF interactions, as well as the nature of the DMMP adsorption sites. Initial IR profiles for all UiO-67-X share similar spectrum characteristics yielding several well-defined features previously assigned for low-defect and highly crystalline structures (Figure 5, black).[21,26−28] Linker functionalization is confirmed by the presence of signature vibrational features associated with asymmetric/symmetric stretching of the amino (3485/3398 cm^{-1}) and methyl (2962/2852 cm^{-1}) groups for UiO-67-NH_2 and UiO-67-CH_3, respectively.[95,96] Full IR spectra of the pristine samples are provided in the Supporting Information in Figure S22. All IR spectra are reported for samples activated at 473 K.

In situ IR monitoring during the adsorption process probes the initial interactions of DMMP at 100 K. Upon exposure

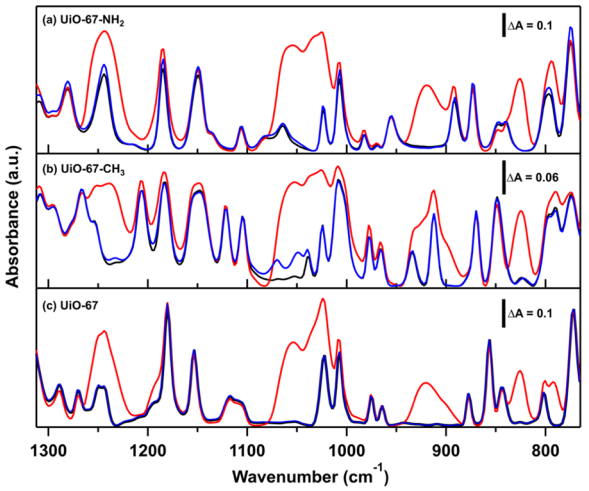

Figure 5. FTIR spectra of the fingerprint region for (a) UiO-67-NH_2, (b) UiO-67-CH_3, and (c) UiO-67 showing the initial MOF before DMMP exposure (black), after a 9000 L DMMP exposure (red), and after thermal treatment to 473 K (blue). All spectra were collected at 100 K and baseline corrected.

(9000 L), several bands characteristic of DMMP evolve within the 1300−800 cm^{-1} region (Figure 5, red), while the features associated with the clean MOF remain unperturbed (Figure 5, black). For the UiO-67 spectrum, bands centered at 1245, 1054, 1024, and 920 cm^{-1} are assigned to P═O stretching, asymmetric and symmetric O−C stretching, and P−CH_3 bending of DMMP in the MOF, respectively (Figure 5, red).[97−100] Exposure at 100 K leads to a significant (30−40 cm^{-1}) red shift for ν(P═O) and ν(O−C) modes compared to that of gaseous DMMP, while the remaining DMMP spectral features remain largely unaffected, suggesting that coordination occurs primarily through the phosphoryl oxygen and/or the methoxy moieties. This observation is in qualitative agreement with the highest binding energy configurations observed in Figure 1, where the closest distances between DMMP and framework atoms involve O atoms within DMMP interacting with H atoms of the framework. Chemisorption of DMMP on Zr-based MOFs has been identified by a large shift in the phosphoryl stretching frequency from 1276 to 1188 cm^{-1}.[21] In the present work, the phosphoryl stretch only shifts to 1245 cm^{-1}, indicating a weaker (physisorption) interaction. This could be due to the relatively low density of defects in the MOFs synthesized in this work, because the chemisorption of DMMP on the SBU requires the presence of undercoordinated Zr sites not available in nondefective UiO-67. A complete assignment of DMMP vibrational modes for all UiO-67-X is provided in Table 2.

Temperature-programmed IR experiments record DMMP−MOF interactions as samples are heated following DMMP exposure. Complete removal of DMMP is observed by 473 K for UiO-67 and UiO-67-NH_2 (Figure 5a,c), as evidenced by the disappearance of characteristic DMMP features described previously and recovery of pristine MOF spectral features. The recovery of the clean MOF spectra upon cooling to 100 K indicates completely reversible adsorption of DMMP on both UiO-67 and UiO-67-NH_2. However, for UiO-67-CH_3, spectral features potentially consistent with adsorbed DMMP are observed at 1070 and 1049 cm^{-1} following thermal treatment to 473 K (Figure 5b). These features may be associated with asymmetric and symmetric methoxy stretch modes, ν(O−C).

DOI: 10.1021/acs.jpcc.9b05574
J. Phys. Chem. C 2019, 123, 19748−19758

Table 2. Assignment of DMMP Infrared Vibrational Modes (cm^{-1}) in Gas Phase (298 K)[a] and Adsorbed on UiO-67 Series MOFs (100 K)[b]

vibrational mode[a]	gas-phase 298 K[a]	UiO-67-NH_2 100 K	UiO-67-CH_3 100 K	UiO-67 100 K
$\nu_{as}(P-CH_3)$	3014	2990	2994	2990
$\nu_{as}(O-CH_3)$	2962	2960	2959	2960
$\nu_{s}(P-CH_3)$	2921	2924	2923	2924
$\nu_{s}(O-CH_3)$	2859	2853	2850	2853
$\delta_{as}(O-CH_3)$	1471	1467	1466	1465
$\delta_{s}(P-CH_3)$	1315	1316	1317	1319
$\nu(P{=}O)$	1276	1244	1238	1244
$\rho(O-CH_3)$	1188	1191	1192	1187
$\nu_{a}(O-C)$	1075	1051	1050	1054
$\nu_{s}(O-C)$	1050	1031	1030	1032
$\rho(P-CH_3)$	919	919	921	920

[a]Vibrational assignments and gas-phase frequencies.[97−100] [b]ν = stretch, ρ = bend, δ = deformation, as = asymmetric, s = symmetric.

During exposure at 100 K, these features were observed at 1050 and 1030 cm^{-1}. The shift toward higher frequency, essentially the gas-phase values, suggests residual gas-phase-like DMMP in UiO-67-CH_3 after thermal treatment. We do not have an explanation for this feature, but we note that it is not consistent with chemisorbed DMMP.

CONCLUSIONS

Density functional theory has been used to predict ligand functionalizations that yield differential uptake of DMMP in a UiO-67 family MOF.[21] Three functionalized MOFs were synthesized based on DFT predictions of differential binding energies. TPD experiments showed that the functionalized MOFs indeed exhibit the same order of adsorption affinities for DMMP predicted from DFT calculations and classical GCMC simulations. Consistent with the TPD studies discussed above, FTIR showed no evidence of decomposition reactions of DMMP with any of the MOFs, in contrast to other literature accounts, though a small amount of DMMP persists for UiO-67-CH_3, even after heating to 473 K. These results demonstrate that functionalized MOF domains with a differential affinity for CWAs can be fabricated, providing a foundation on which stratified MOFs for CWA capture may be based. Our calculations and experiments predict that a stratified MOF consisting of UiO-67-NH_2 ⊂ UiO-67-CH_3 ⊂ UiO-67 will show an equilibrium concentration gradient of DMMP induced by the differential binding of DMMP. Assuming a Boltzmann distribution, the ratio of concentrations is predicted to be about 55:17:1 in the UiO-67-NH_2, UiO-67-CH_3, and UiO-67 strata, respectively, based on the DFT energies (Table 1) at a temperature of 300 K (details of the calculation given in the Supporting Information). Thus, even these modest differences in binding energies can result in a significant concentration enhancement in a target stratum of a stratified MOF.

ASSOCIATED CONTENT

Supporting Information

The Supporting Information is available free of charge on the ACS Publications website at DOI: 10.1021/acs.jpcc.9b05574.

Synthesis procedures, binding energies calculated between DMMP and functional groups, bond stretch and bond-bend parameters for the DMMP molecule, helium void fractions, optimal geometries from density functional theory, and detailed analysis procedures (PDF)

AUTHOR INFORMATION

Corresponding Authors

*E-mail: eborguet@temple.edu (E.B.).
*E-mail: nrosi@pitt.edu (N.L.R.).
*E-mail: karlj@pitt.edu (J.K.J.).

ORCID

Tian-Yi Luo: 0000-0002-9973-9328
Eric Borguet: 0000-0003-0593-952X
Nathaniel L. Rosi: 0000-0001-8025-8906
J. Karl Johnson: 0000-0002-3608-8003

Present Address

⊥Unite de Catalyse et Chimie du Solide (UCCS)-UMR CNRS 8181, Universite de Lille, Bat. C3- Cite scientifique, 59655 Villeneuve d'Ascq, France (M.R.).

Author Contributions

∥J.P.R., I.G., and T.-Y.L. contributed equally to this work.

Notes

The authors declare no competing financial interest.

ACKNOWLEDGMENTS

The authors thank the University of Illinois, Department of Chemistry Microanalytical Laboratory, for completing elemental microanalyses. The authors also thank the Peterson Nanoscale Fabrication and Characterization Facility at the University of Pittsburgh for provision of access to powder XRD and transmission electron microscopy instrumentation, and Avery Green and Carl Ventrice for providing LabVIEW code to run TPD experiments. Computations were performed at the University of Pittsburgh's Center for Research Computing, the Pittsburgh Supercomputer Center through a grant from the Extreme Science and Engineering Discovery Environment (XSEDE), which is supported by the National Science Foundation grant number ACI-1548562, under allocation No. TG-DMR110091, and the U.S. Army Engineer Research and Development Center DoD Supercomputer Resource Center. This project received support from the Defense Threat Reduction Agency (DTRA) (Grant no. HDTRA1-16-1-0044).

DOI: 10.1021/acs.jpcc.9b05574
J. Phys. Chem. C 2019, 123, 19748−19758

REFERENCES

(1) Jacoby, M. Air Filters for the Face. *Chem. Eng. News Archive* **2014**, *92* (49), 34−38, DOI: 10.1021/cen-09249-scitech1.

(2) Morrison, R. W. *Overview of Current Collective Protection Filtration Technology*, NBC Defense Collective Protection Conference, 2002.

(3) Prasad, G.; Singh, B.; Vijayaraghavan, R. Respiratory Protection against Chemical and Biological Warfare Agents. *Def. Sci. J.* **2008**, *58*, 686.

(4) Bobbitt, N. S.; Mendonca, M. L.; Howarth, A. J.; Islamoglu, T.; Hupp, J. T.; Farha, O. K.; Snurr, R. Q. Metal−Organic Frameworks for the Removal of Toxic Industrial Chemicals and Chemical Warfare Agents. *Chem. Soc. Rev.* **2017**, *46*, 3357−3385.

(5) Linders, M. J. G.; Baak, P. J.; van Bokhoven, J. J. G. M. Exploratory Investigation of the Risk of Desorption from Activated Carbon Filters in Respiratory Protective Devices. *Ind. Eng. Chem. Res.* **2007**, *46*, 4034−4039.

(6) *Adsorption and Desorption of Chemical Warfare Agents on Activated Carbon: Impact of Temperature and Relative Humidity*; U.S. Environmental Protection Agency: Washington D.C., 2014.

(7) Liao, P.-Q.; Huang, N.-Y.; Zhang, W.-X.; Zhang, J.-P.; Chen, X.-M. Controlling Guest Conformation for Efficient Purification of Butadiene. *Science* **2017**, *356*, 1193−1196.

(8) Herm, Z. R.; Wiers, B. M.; Mason, J. A.; van Baten, J. M.; Hudson, M. R.; Zajdel, P.; Brown, C. M.; Masciocchi, N.; Krishna, R.; Long, J. R. Separation of Hexane Isomers in a Metal-Organic Framework with Triangular Channels. *Science* **2013**, *340*, 960−964.

(9) Li, T.; Chen, D.-L.; Sullivan, J. E.; Kozlowski, M. T.; Johnson, J. K.; Rosi, N. L. Systematic Modulation and Enhancement of CO_2: N_2 Selectivity and Water Stability in an Isoreticular Series of bio-MOF-11 Analogues. *Chem. Sci.* **2013**, *4*, 1746−1755.

(10) Fracaroli, A. M.; Furukawa, H.; Suzuki, M.; Dodd, M.; Okajima, S.; Gándara, F.; Reimer, J. A.; Yaghi, O. M. Metal−Organic Frameworks with Precisely Designed Interior for Carbon Dioxide Capture in the Presence of Water. *J. Am. Chem. Soc.* **2014**, *136*, 8863−8866.

(11) Ploskonka, A. M.; DeCoste, J. B. Tailoring the Adsorption and Reaction Chemistry of the Metal−Organic Frameworks UiO-66, UiO-66-NH_2, and HKUST-1 via the Incorporation of Molecular Guests. *ACS Appl. Mater. Interfaces* **2017**, *9*, 21579−21585.

(12) de Koning, M. C.; van Grol, M.; Breijaert, T. Degradation of Paraoxon and the Chemical Warfare Agents VX, Tabun, and Soman by the Metal−Organic Frameworks UiO-66-NH_2, MOF-808, NU-1000, and PCN-777. *Inorg. Chem.* **2017**, *56*, 11804−11809.

(13) Liu, Y.; Howarth, A. J.; Hupp, J. T.; Farha, O. K. Selective Photooxidation of a Mustard-Gas Simulant Catalyzed by a Porphyrinic Metal−Organic Framework. *Angew. Chem., Int. Ed.* **2015**, *54*, 9001−9005.

(14) Liu, Y.; Buru, C. T.; Howarth, A. J.; Mahle, J. J.; Buchanan, J. H.; DeCoste, J. B.; Hupp, J. T.; Farha, O. K. Efficient and Selective Oxidation of Sulfur Mustard Using Singlet Oxygen Generated by a Pyrene-based Metal−Organic Framework. *J. Mater. Chem. A* **2016**, *4*, 13809−13813.

(15) Bromberg, L.; Klichko, Y.; Chang, E. P.; Speakman, S.; Straut, C. M.; Wilusz, E.; Hatton, T. A. Alkylaminopyridine-Modified Aluminum Aminoterephthalate Metal-Organic Frameworks As Components of Reactive Self-Detoxifying Materials. *ACS Appl. Mater. Interfaces* **2012**, *4*, 4595−4602.

(16) Mondloch, J. E.; Katz, M. J.; Isley Iii, W. C.; Ghosh, P.; Liao, P.; Bury, W.; Wagner, G. W.; Hall, M. G.; DeCoste, J. B.; Peterson, G. W.; Snurr, R. Q.; Cramer, C. J.; Hupp, J. T.; Farha, O. K. Destruction of Chemical Warfare Agents Using Metal−Organic Frameworks. *Nat. Mater.* **2015**, *14*, 512.

(17) Katz, M. J.; Mondloch, J. E.; Totten, R. K.; Park, J. K.; Nguyen, S. T.; Farha, O. K.; Hupp, J. T. Simple and Compelling Biomimetic Metal−Organic Framework Catalyst for the Degradation of Nerve Agent Simulants. *Angew. Chem., Int. Ed.* **2014**, *53*, 497−501.

(18) Katz, M. J.; Moon, S.-Y.; Mondloch, J. E.; Beyzavi, M. H.; Stephenson, C. J.; Hupp, J. T.; Farha, O. K. Exploiting Parameter Space in MOFs: a 20-Fold Enhancement of Phosphate-Ester Hydrolysis with UiO-66-NH_2. *Chem. Sci.* **2015**, *6*, 2286−2291.

(19) Gil-San-Millan, R.; López-Maya, E.; Hall, M.; Padial, N. M.; Peterson, G. W.; DeCoste, J. B.; Rodríguez-Albelo, L. M.; Oltra, J. E.; Barea, E.; Navarro, J. A. R. Chemical Warfare Agents Detoxification Properties of Zirconium Metal−Organic Frameworks by Synergistic Incorporation of Nucleophilic and Basic Sites. *ACS Appl. Mater. Interfaces* **2017**, *9*, 23967−23973.

(20) Zhao, J.; Lee, D. T.; Yaga, R. W.; Hall, M. G.; Barton, H. F.; Woodward, I. R.; Oldham, C. J.; Walls, H. J.; Peterson, G. W.; Parsons, G. N. Ultra-Fast Degradation of Chemical Warfare Agents Using MOF−Nanofiber Kebabs. *Angew. Chem., Int. Ed.* **2016**, *55*, 13224−13228.

(21) Wang, G.; Sharp, C.; Plonka, A. M.; Wang, Q.; Frenkel, A. I.; Guo, W.; Hill, C.; Smith, C.; Kollar, J.; Troya, D.; Morris, J. R. Mechanism and Kinetics for Reaction of the Chemical Warfare Agent Simulant, DMMP(g), with Zirconium(IV) MOFs: an Ultrahigh-Vacuum and DFT Study. *J. Phys. Chem. C* **2017**, *121*, 11261−11272.

(22) DeCoste, J. B.; Rossin, J. A.; Peterson, G. W. Hierarchical Pore Development by Plasma Etching of Zr-Based Metal−Organic Frameworks. *Chem. - Eur. J.* **2015**, *21*, 18029−18032.

(23) Mondal, S. S.; Holdt, H.-J. Breaking Down Chemical Weapons by Metal−Organic Frameworks. *Angew. Chem., Int. Ed.* **2016**, *55*, 42−44.

(24) Lee, D. T.; Zhao, J.; Oldham, C. J.; Peterson, G. W.; Parsons, G. N. UiO-66-NH_2 Metal−Organic Framework (MOF) Nucleation on TiO_2, ZnO, and Al_2O_3 Atomic Layer Deposition-Treated Polymer Fibers: Role of Metal Oxide on MOF Growth and Catalytic Hydrolysis of Chemical Warfare Agent Simulants. *ACS Appl. Mater. Interfaces* **2017**, *9*, 44847−44855.

(25) López-Maya, E.; Montoro, C.; Rodríguez-Albelo, L. M.; Aznar Cervantes, S. D.; Lozano-Pérez, A. A.; Cenís, J. L.; Barea, E.; Navarro, J. A. R. Textile/Metal−Organic-Framework Composites as Self-Detoxifying Filters for Chemical-Warfare Agents. *Angew. Chem., Int. Ed.* **2015**, *54*, 6790−6794.

(26) Cavka, J. H.; Jakobsen, S.; Olsbye, U.; Guillou, N.; Lamberti, C.; Bordiga, S.; Lillerud, K. P. A New Zirconium Inorganic Building Brick Forming Metal Organic Frameworks with Exceptional Stability. *J. Am. Chem. Soc.* **2008**, *130*, 13850−13851.

(27) DeCoste, J. B.; Peterson, G. W.; Jasuja, H.; Glover, T. G.; Huang, Y.-g.; Walton, K. S. Stability and Degradation Mechanisms of Metal−Organic Frameworks Containing the $Zr_6O_4(OH)_4$ Secondary Building Unit. *J. Mater. Chem. A* **2013**, *1*, 5642−5650.

(28) Valenzano, L.; Civalleri, B.; Chavan, S.; Bordiga, S.; Nilsen, M. H.; Jakobsen, S.; Lillerud, K. P.; Lamberti, C. Disclosing the Complex Structure of UiO-66 Metal Organic Framework: A Synergic Combination of Experiment and Theory. *Chem. Mater.* **2011**, *23*, 1700−1718.

(29) Kandiah, M.; Nilsen, M. H.; Usseglio, S.; Jakobsen, S.; Olsbye, U.; Tilset, M.; Larabi, C.; Quadrelli, E. A.; Bonino, F.; Lillerud, K. P. Synthesis and Stability of Tagged UiO-66 Zr-MOFs. *Chem. Mater.* **2010**, *22*, 6632−6640.

(30) Kutzscher, C.; Nickerl, G.; Senkovska, I.; Bon, V.; Kaskel, S. Proline Functionalized UiO-67 and UiO-68 Type Metal−Organic Frameworks Showing Reversed Diastereoselectivity in Aldol Addition Reactions. *Chem. Mater.* **2016**, *28*, 2573−2580.

(31) Biswas, S.; Van Der Voort, P. A General Strategy for the Synthesis of Functionalised UiO-66 Frameworks: Characterisation, Stability and CO_2 Adsorption Properties. *Eur. J. Inorg. Chem.* **2013**, *2013*, 2154−2160.

(32) Øien-Ødegaard, S.; Bouchevreau, B.; Hylland, K.; Wu, L.; Blom, R.; Grande, C.; Olsbye, U.; Tilset, M.; Lillerud, K. P. UiO-67-type Metal−Organic Frameworks with Enhanced Water Stability and Methane Adsorption Capacity. *Inorg. Chem.* **2016**, *55*, 1986−1991.

(33) Peterson, G. W.; Destefano, M. R.; Garibay, S. J.; Ploskonka, A.; McEntee, M.; Hall, M.; Karwacki, C. J.; Hupp, J. T.; Farha, O. K. Optimizing Toxic Chemical Removal through Defect-Induced UiO-66-NH_2 Metal−Organic Framework. *Chem. - Eur. J.* **2017**, *23*, 15913−15916.

DOI: 10.1021/acs.jpcc.9b05574
J. Phys. Chem. C 2019, 123, 19748−19758

(34) Moon, S.-Y.; Wagner, G. W.; Mondloch, J. E.; Peterson, G. W.; DeCoste, J. B.; Hupp, J. T.; Farha, O. K. Effective, Facile, and Selective Hydrolysis of the Chemical Warfare Agent VX Using Zr6-Based Metal−Organic Frameworks. *Inorg. Chem.* **2015**, *54*, 10829−10833.
(35) Trickett, C. A.; Gagnon, K. J.; Lee, S.; Gándara, F.; Bürgi, H.-B.; Yaghi, O. M. Definitive Molecular Level Characterization of Defects in UiO-66 Crystals. *Angew. Chem., Int. Ed.* **2015**, *54*, 11162−11167.
(36) Luo, T.-Y.; Liu, C.; Gan, X. Y.; Muldoon, P. F.; Diemler, N. A.; Millstone, J. E.; Rosi, N. L. Multivariate Stratified Metal−Organic Frameworks: Diversification Using Domain Building Blocks. *J. Am. Chem. Soc.* **2019**, *141*, 2161−2168.
(37) Wu, H.; Yildirim, T.; Zhou, W. Exceptional Mechanical Stability of Highly Porous Zirconium Metal−Organic Framework UiO-66 and Its Important Implications. *J. Phys. Chem. Lett.* **2013**, *4*, 925−930.
(38) Lawrence, M. C.; Schneider, C.; Katz, M. J. Determining the Structural Stability of UiO-67 with Respect to Time: A Solid-State NMR Investigation. *Chem. Commun.* **2016**, *52*, 4971−4974.
(39) Katz, M. J.; Brown, Z. J.; Colón, Y. J.; Siu, P. W.; Scheidt, K. A.; Snurr, R. Q.; Hupp, J. T.; Farha, O. K. A Facile Synthesis of UiO-66, UiO-67 and Their Derivatives. *Chem. Commun.* **2013**, *49*, 9449−9451.
(40) Vermoortele, F.; Vandichel, M.; Van de Voorde, B.; Ameloot, R.; Waroquier, M.; Van Speybroeck, V.; De Vos, D. E. Electronic Effects of Linker Substitution on Lewis Acid Catalysis with Metal−Organic Frameworks. *Angew. Chem., Int. Ed.* **2012**, *51*, 4887−4890.
(41) Kim, M.; Cahill, J. F.; Su, Y.; Prather, K. A.; Cohen, S. M. Postsynthetic Ligand Exchange as A Route to Functionalization of 'Inert' Metal−Organic Frameworks. *Chem. Sci.* **2012**, *3*, 126−130.
(42) DeStefano, M. R.; Islamoglu, T.; Garibay, S. J.; Hupp, J. T.; Farha, O. K. Room-Temperature Synthesis of UiO-66 and Thermal Modulation of Densities of Defect Sites. *Chem. Mater.* **2017**, *29*, 1357−1361.
(43) Zhang, J.; Dolg, M. ABCluster: the Artificial Bee Colony Algorithm for Cluster Global Optimization. *Phys. Chem. Chem. Phys.* **2015**, *17*, 24173−24181.
(44) Zhang, J.; Dolg, M. Global Optimization of Clusters of Rigid Molecules Using the Artificial Bee Colony Algorithm. *Phys. Chem. Chem. Phys.* **2016**, *18*, 3003−3010.
(45) Neese, F. The ORCA Program System. *Wiley Interdiscip. Rev.: Comput. Mol. Sci.* **2012**, *2*, 73−78.
(46) Perdew, J. P.; Burke, K.; Ernzerhof, M. Generalized Gradient Approximation Made Simple. *Phys. Rev. Lett.* **1996**, *77*, 3865−3868.
(47) Weigend, F.; Ahlrichs, R. Balanced Basis Sets of Split Valence, Triple Zeta Valence and Quadruple Zeta Valence Quality for H to Rn: Design and Assessment of Accuracy. *Phys. Chem. Chem. Phys.* **2005**, *7*, 3297−3305.
(48) Weigend, F. Accurate Coulomb-Fitting Basis Sets for H to Rn. *Phys. Chem. Chem. Phys.* **2006**, *8*, 1057−1065.
(49) Grimme, S.; Antony, J.; Ehrlich, S.; Krieg, H. A Consistent and Accurate ab initio Parametrization of Density Functional Dispersion Correction (DFT-D) for the 94 Elements H-Pu. *J. Chem. Phys.* **2010**, *132*, No. 154104.
(50) Grimme, S.; Ehrlich, S.; Goerigk, L. Effect of the Damping Function in Dispersion Corrected Density Functional Theory. *J. Comput. Chem.* **2011**, *32*, 1456−1465.
(51) Boys, S. F.; Bernardi, F. The Calculation of Small Molecular Interactions by the Differences of Separate Total Energies. Some Procedures with Reduced Errors. *Mol. Phys.* **1970**, *19*, 553−566.
(52) Frisch, M.; Trucks, G.; Schlegel, H.; Scuseria, G.; Robb, M.; Cheeseman, J.; Scalmani, G.; Barone, V.; Mennucci, B.; Petersson, G. et al. *Gaussian 09*; Gaussian, Inc., 2014.
(53) Guo, Y.; Riplinger, C.; Becker, U.; Liakos, D. G.; Minenkov, Y.; Cavallo, L.; Neese, F. Communication: an Improved Linear Scaling Perturbative Triples Correction for the Domain Based Local Pair-Natural Orbital Based Singles and Doubles Coupled Cluster Method [DLPNO-CCSD(T)]. *J. Chem. Phys.* **2018**, *148*, No. 011101.
(54) Frigo, M.; Johnson, S. G. The Design and Implementation of FFTW3. *Proc. IEEE* **2005**, *93*, 216−231.
(55) VandeVondele, J.; Krack, M.; Mohamed, F.; Parrinello, M.; Chassaing, T.; Hutter, J. Quickstep: Fast and Accurate Density Functional Calculations Using a Mixed Gaussian and Plane Waves Approach. *Comput. Phys. Commun.* **2005**, *167*, 103−128.
(56) VandeVondele, J.; Hutter, J. An Efficient Orbital Transformation Method for Electronic Structure Calculations. *J. Chem. Phys.* **2003**, *118*, 4365−4369.
(57) Ye, J.; Johnson, J. K. Screening Lewis Pair Moieties for Catalytic Hydrogenation of CO_2 in Functionalized UiO-66. *ACS Catal.* **2015**, *5*, 6219−6229.
(58) Goedecker, S.; Teter, M.; Hutter, J. Separable Dual-space Gaussian Pseudopotentials. *Phys. Rev. B* **1996**, *54*, 1703−1710.
(59) VandeVondele, J.; Hutter, J. Gaussian Basis Sets for Accurate Calculations on Molecular Systems in Gas and Condensed Phases. *J. Chem. Phys.* **2007**, *127*, No. 114105.
(60) Liu, D. C.; Nocedal, J. On the Limited Memory BFGS Method for Large Scale Optimization. *Math. Program.* **1989**, *45*, 503−528.
(61) Ceriotti, M.; Bussi, G.; Parrinello, M. Langevin Equation with Colored Noise for Constant-Temperature Molecular Dynamics Simulations. *Phys. Rev. Lett.* **2009**, *102*, No. 020601.
(62) Ceriotti, M.; Bussi, G.; Parrinello, M. Nuclear Quantum Effects in Solids Using a Colored-Noise Thermostat. *Phys. Rev. Lett.* **2009**, *103*, No. 030603.
(63) Rowley, L. A.; Nicholson, D.; Parsonage, N. G. Monte Carlo Grand Canonical Ensemble Calculation in A Gas-Liquid Transition Region for 12-6 Argon. *J. Comput. Phys.* **1975**, *17*, 401−414.
(64) Düren, T.; Millange, F.; Férey, G.; Walton, K. S.; Snurr, R. Q. Calculating Geometric Surface Areas as a Characterization Tool for Metal−Organic Frameworks. *J. Phys. Chem. C* **2007**, *111*, 15350−15356.
(65) Brunauer, S.; Emmett, P. H.; Teller, E. Adsorption of Gases in Multimolecular Layers. *J. Am. Chem. Soc.* **1938**, *60*, 309−319.
(66) Dubbeldam, D.; Calero, S.; Ellis, D. E.; Snurr, R. Q. RASPA: Molecular Simulation Software for Adsorption and Diffusion in Flexible Nanoporous Materials. *Mol. Simul.* **2016**, *42*, 81−101.
(67) Potoff, J. J.; Siepmann, J. I. Vapor−Liquid Equilibria of Mixtures Containing Alkanes, Carbon Dioxide, and Nitrogen. *AlChE J.* **2001**, *47*, 1676−1682.
(68) Sokkalingam, N.; Kamath, G.; Coscione, M.; Potoff, J. J. Extension of the Transferable Potentials for Phase Equilibria Force Field to Dimethylmethyl Phosphonate, Sarin, and Soman. *J. Phys. Chem. B* **2009**, *113*, 10292−10297.
(69) Vishnyakov, A.; Neimark, A. V. Molecular Model of Dimethylmethylphosphonate and Its Interactions with Water. *J. Phys. Chem. A* **2004**, *108*, 1435−1439.
(70) Vanduyfhuys, L.; Vandenbrande, S.; Verstraelen, T.; Schmid, R.; Waroquier, M.; Van Speybroeck, V. QuickFF: A program for A Quick And Easy Derivation of Force Fields for Metal-Organic Frameworks from ab initio Input. *J. Comput. Chem.* **2015**, *36*, 1015−1027.
(71) A Private Conversation Between J. Karl Johnson, Jonathan Ruffley, Aleksey Vishnyakov and Alexander Neimark on March 5, 2018.
(72) Ewald, P. P. Die Berechnung optischer und elektrostatischer Gitterpotentiale. *Ann. Phys.* **1921**, *369*, 253−287.
(73) Plimpton, S. Fast Parallel Algorithms for Short-Range Molecular Dynamics. *J. Comput. Phys.* **1995**, *117*, 1−19.
(74) Martyna, G. J.; Tobias, D. J.; Klein, M. L. Constant Pressure Molecular Dynamics Algorithms. *J. Chem. Phys.* **1994**, *101*, 4177−4189.
(75) Martínez, L.; Andrade, R.; Birgin, E. G.; Martínez, J. M. PACKMOL: A Package for Building Initial Configurations for Molecular Dynamics Simulations. *J. Comput. Chem.* **2009**, *30*, 2157−2164.
(76) Limas, N. G.; Manz, T. A. Introducing DDEC6 Atomic Population Analysis: Part 4. Efficient Parallel Computation of Net

DOI: 10.1021/acs.jpcc.9b05574
J. Phys. Chem. C 2019, 123, 19748−19758

Atomic Charges, Atomic Spin Moments, Bond Orders, and More. *RSC Adv.* **2018**, *8*, 2678−2707.
(77) Manz, T. A. Introducing DDEC6 Atomic Population Analysis: Part 3. Comprehensive Method to Compute Bond Orders. *RSC Adv.* **2017**, *7*, 45552−45581.
(78) Limas, N. G.; Manz, T. A. Introducing DDEC6 Atomic Population Analysis: Part 2. Computed Results for A Wide Range of Periodic and Nonperiodic Materials. *RSC Adv.* **2016**, *6*, 45727−45747.
(79) Manz, T. A.; Limas, N. G. Introducing DDEC6 Atomic Population Analysis: Part 1. Charge Partitioning Theory and Methodology. *RSC Adv.* **2016**, *6*, 47771−47801.
(80) Mayo, S. L.; Olafson, B. D.; Goddard, W. A. DREIDING: A Generic Force Field for Molecular Simulations. *J. Phys. Chem. A* **1990**, *94*, 8897−8909.
(81) Rappe, A. K.; Casewit, C. J.; Colwell, K. S.; Goddard, W. A.; Skiff, W. M. UFF, A Full Periodic Table Force Field for Molecular Mechanics and Molecular Dynamics Simulations. *J. Am. Chem. Soc.* **1992**, *114*, 10024−10035.
(82) Ye, J.; Johnson, J. K. Catalytic Hydrogenation of CO_2 to Methanol in A Lewis Pair Functionalized MOF. *Catal. Sci. Technol.* **2016**, *6*, 8392−8405.
(83) Allen, M. P.; Tildesley, D. J. *Computer Simulation of Liquids*; Oxford University Press, 2017.
(84) Kwon, S.; Vidic, R.; Borguet, E. The Effect of Surface Chemical Functional Groups on the Adsorption and Desorption of A Polar Molecule, Acetone, from A Model Carbonaceous Surface, Graphite. *Surf. Sci.* **2003**, *522*, 17−26.
(85) Stukowski, A. Visualization and Analysis of Atomistic Simulation Data with OVITO−the Open Visualization Tool. *Modell. Simul. Mater. Sci. Eng.* **2009**, *18*, No. 015012.
(86) Thommes, M.; Kaneko, K.; Neimark Alexander, V.; Olivier James, P.; Rodriguez-Reinoso, F.; Rouquerol, J.; Sing Kenneth, S. W. Physisorption of Gases, with Special Reference to the Evaluation of Surface Area and Pore Size Distribution (IUPAC Technical Report). *Pure Appl. Chem.* **2015**, *87*, 1051.
(87) Holtzclaw, J. R.; Wyatt, J. R.; Campana, J. E. Structure and Fragmentation of Dimethyl Methylphosphonate and Trimethyl Phosphite. *Org. Mass Spectrom.* **1985**, *20*, 90−97.
(88) Smentkowski, V. S.; Hagans, P.; Yates, J. T. Study of the Catalytic Destruction of Dimethyl Methylphosphonate(DMMP): Oxidation over Molybdenum(110). *J. Phys. Chem. A* **1988**, *92*, 6351−6357.
(89) Gutsev, G. L.; Ampadu Boateng, D.; Jena, P.; Tibbetts, K. M. A Theoretical and Mass Spectrometry Study of Dimethyl Methylphosphonate: New Isomers and Cation Decay Channels in an Intense Femtosecond Laser Field. *J. Phys. Chem. A* **2017**, *121*, 8414−8424.
(90) Burke, D. J.; Wolff, A. J.; Edridge, J. L.; Brown, W. A. The Adsorption and Desorption of Ethanol Ices from A Model Grain Surface. *J. Chem. Phys.* **2008**, *128*, No. 104702.
(91) Green, S. D.; Bolina, A. S.; Chen, R.; Collings, M. P.; Brown, W. A.; McCoustra, M. R. S. Applying Laboratory Thermal Desorption Data in an Interstellar Context: Sublimation of Methanol Thin Films. *Mon. Not. R. Astron. Soc.* **2009**, *398*, 357−367.
(92) Redhead, P. A. Thermal Desorption of Gases. *Vacuum* **1962**, *12*, 203−211.
(93) de Jong, A. M.; Niemantsverdriet, J. W. Thermal Desorption Analysis: Comparative Test of Ten Commonly Applied Procedures. *Surf. Sci.* **1990**, *233*, 355−365.
(94) Campbell, C. T.; Sellers, J. R. V. Enthalpies and Entropies of Adsorption on Well-Defined Oxide Surfaces: Experimental Measurements. *Chem. Rev.* **2013**, *113*, 4106−4135.
(95) Peterson, G. W.; Mahle, J. J.; DeCoste, J. B.; Gordon, W. O.; Rossin, J. A. Extraordinary NO_2 Removal by the Metal−Organic Framework UiO-66-NH_2. *Angew. Chem., Int. Ed.* **2016**, *55*, 6235−6238.
(96) Huang, Y.; Qin, W.; Li, Z.; Li, Y. Enhanced Stability and CO_2 Affinity of A UiO-66 Type Metal−Organic Framework Decorated with Dimethyl Groups. *Dalton Trans.* **2012**, *41*, 9283−9285.
(97) Bertilsson, L.; Engquist, I.; Liedberg, B. Interaction of Dimethyl Methylphosphonate with Alkanethiolate Monolayers Studied by Temperature-Programmed Desorption and Infrared Spectroscopy. *J. Phys. Chem. B* **1997**, *101*, 6021−6027.
(98) Moss, J. A.; Szczepankiewicz, S. H.; Park, E.; Hoffmann, M. R. Adsorption and Photodegradation of Dimethyl Methylphosphonate Vapor at TiO_2 Surfaces. *J. Phys. Chem. B* **2005**, *109*, 19779−19785.
(99) Rusu, C. N.; Yates, J. T. Adsorption and Decomposition of Dimethyl Methylphosphonate on TiO_2. *J. Phys. Chem. B* **2000**, *104*, 12292−12298.
(100) Hung, W.-C.; Wang, J.-C.; Wu, K.-H. Adsorption and Decomposition of Dimethyl Methylphosphonate (DMMP) on Expanded Graphite/Metal Oxides. *Appl. Surf. Sci.* **2018**, *444*, 330−335.

DOI: 10.1021/acs.jpcc.9b05574
J. Phys. Chem. C 2019, 123, 19748−19758